



Combined experimental and theoretical approach to improve measurement accuracy of temperature-dependent reflectance of copper for near-infrared lasers

Manuel Mattern¹ · Lalit Mohan Kukreja^{1,2} · Andreas Ostendorf¹

Received: 6 September 2023 / Accepted: 18 December 2023 / Published online: 8 January 2024
© The Author(s) 2024

Abstract

The low process stability of laser welding of copper with near-infrared lasers requires precise input data for process control and meaningful simulations. But meanwhile, available datasets of temperature-dependent reflectance or absorptance for near-infrared lasers on copper do not show good agreement between the different sources and often do not include the fusion process, which is of crucial importance for realistic laser welding simulations. Additionally, most of the datasets are only calculated. Therefore, in a previous study, temperature-dependent reflectance measurements were performed on electro tough-pitch copper using a near-infrared laser. The measurements revealed a reflectance drift, which was induced by the setup behavior during heating, and the time-dependence of chemical reactions like the redox-reaction as possible error sources. In this study, experiments on laser melting as the fundamental process of laser welding were performed, together with corresponding simulations using the measured reflectance values for oxide-reduced and for untreated copper from the previous study. Then, the simulations were compared with the experiments to estimate the accuracy of the reflectance measurements. To provide context, the same simulations were also conducted using reflectance datasets from other authors. In a second step, the reflectance data were corrected with respect to the reflectance drift and the effects of redox reactions were adapted to the conditions of the laser melting experiments. Using the resulting reflectance curves, an improved agreement of simulation results and the experiments was achieved over a range of different test cases, without the necessity of correction factors in the simulation model.

Keywords Copper · Reflectance · Temperature · Oxidation · Simulation · Melting

1 Introduction

Copper is well-known for its excellent electrical and thermal conductivities of 58.5 MS/m and 398 W/(m*K) [1]. This makes it the material of choice in a variety of electrical and thermal applications [2–5]. But copper is also known to cause a low process stability when used in welding applications with near-infrared lasers [6–8]. For a detailed analysis

of the reasons and to develop strategies to improve the process stability, process simulations play an important role [6, 9]. Since the process window is known to be narrow, a meaningful simulation of the process requires accurate input data, especially with respect to the temperature-dependent absorptance, which plays an important role for the process reproducibility. As is well known, the absorptance A can either be given directly, or it can be derived from the reflectance R by calculating

$$A = 1 - R \quad (1)$$

Several studies on the temperature-dependent absorptance or reflectance of copper have been published [10–16]. But most of the published datasets are only calculated and some do not include the abrupt increase in the absorptance at melting temperature. While certain studies [11, 12, 14, 15] include a magnitude for the abrupt increase in the absorptance at melting temperature, none of them is clearly

Recommended for publication by Commission IV - Power Beam Processes

✉ Manuel Mattern
manuel.mattern@ruhr-uni-bochum.de

¹ Ruhr-University Bochum, Applied Laser Technologies, Universitätsstr. 150, 44801 Bochum, Germany

² Epi-knowledge Foundation, C2 – 4/1:3, Sector - 4, Vashi, Navi Mumbai 400703, India

based on measurements. Additionally, the relative deviations between the absorptance values given in or derived from the different sources are of a substantial magnitude without obvious reasons. The temperature-dependent reflectance measurements in a previous study of the authors [17] were carried out to fill this gap. They were conducted on cold rolled sheets of electro tough-pitch copper (Cu-ETP) with untreated surface, reduced surface, polished surface, or resolidified surface [17]. The sample temperature during the measurements with a 1064 nm laser was controlled by the help of a ceramic heating element [17]. The reflectance measurements were conducted in an integrating sphere, which had several advantages over calorimetric techniques that measure the absorptance [17]. For example, the accuracy of the attributed sample temperature is not affected by significant local energy input at the sample surface, which might even lead to unintended early melting when the sample approaches melting temperature [17]. Also, measurements with the integrating sphere technique can be conducted at significantly higher sampling rates, enabling a higher density of reflectance data points over temperature, whereas ISO 11551:2019 recommends to keep the sample temperature in calorimetric measurements constant for a duration of about 4 min per measurement, as was already pointed out in [17]. With respect to the data quality, it is generally promising that the measured reflectance values of [17] had the best agreement with the values from the only two measurement-related datasets of the literature, which were Quimby et al. [13] for solid copper, and Kohl et al. [16] for liquid copper. However, the agreement was neither close to perfect, nor was the measurement quality of the two datasets from literature known. While this agreement indicated that the measurement values might be in the right region, an approximate agreement of the unvalidated reflectance values from [17] with other unvalidated reflectance values does not allow to determine or estimate measurement errors. It also remains unclear, if the measurement results of [17] really represent the measured samples better or worse than the literature values do, which is an important question for the selection of the best input data for process simulations of laser welding.

In the publication of [17], an error for the measured reflectance was identified in the form of a signal drift that was induced by an increase of the setup temperature. However, while the measurement data allowed to clearly show the existence and direction of the drift, they did not allow to give the exact magnitude of this error [17]. Besides this measurement error, it was found that the effects of redox reactions depend on the heating rate. The result might be deviating reflectance curves for processes such as laser welding that involve significantly faster heating [17]. Hence, it was recommended to consider the different effect of redox-reactions on the reflectance curve when the data are used

in process simulations [17]. In order to characterize and eventually compensate the measurement error as well as the different effect of the redox-reactions on the measurement data generated by the authors in this previous work, it was suggested to perform a combination of experiments and corresponding simulations that incorporate the measurement data [17].

Since the objective of this study was to analyze and improve the accuracy of the reflectance data and since laser micro-spot welding of copper with near-infrared lasers is known to have a low process repeatability, the experiments were simplified to laser melting, which is the fundamental process of laser welding. This way, the additional instabilities from inhomogeneous welding gap conditions could be avoided in order to focus on the dependence of the experimental results from the different test scenarios. In simulation usage, the standard approach is to make predictions, which are later validated by experiments. In this study, however, the agreement between experimental laser micro-spot melting processes and their corresponding simulations for various process parameters was analyzed in order to optimize the measured reflectance, which was used as input data of the simulation. A better agreement indicates a higher suitability of the simulation for the process. However, the temperature within the laser spot could not be reliably measured during processing, since a thermocouple within the laser spot would affect the absorbed power and might adapt to the surface temperature too slowly. Pyrometers, on the other hand, would be misleading because of the extreme differences in emissivity between oxidized and pure copper. This would lead to substantial errors whenever the surface oxidizes or reduces during the laser pulse, even when ratio pyrometers are used. Therefore, this study refers to the comparison criterion of the required pulse threshold energy to initiate melting of the copper surface. This energy can be determined at good precision by incrementing the pulse energy from spot position to spot position until effects of melting on the sample surface structure become visible. This permanent change can easily be evaluated at any time after the process. Since the melting temperature of copper is a material constant, the pulse threshold energy to melt the copper can be considered equivalent to the pulse energy to reach melting temperature in good approximation. The criterion of the pulse threshold energy to melt the copper also keeps the requirements towards the simulation model simple. This way, the simulation only needs to represent the process up to but not above the melting temperature, which means that uncertainties of the model in the melt regime do not affect the comparison with the experiments. If the geometric parameters of the model and the material parameters like heat conductivity and enthalpy are chosen correctly, the agreement between the simulation result and the experimental result can be taken as an indicator of how good the input reflectance data represent

the temperature-dependent reflectance data in the laser melting process.

This study consisted of two parts: In the first part, simulations were conducted using the unmanipulated reflectance data from the previous study in [17]. The predicted pulse energy threshold required to reach melting temperature at the surface of the sample was compared to the energy that was needed to initiate the same effect in the experiment. The same simulations were repeated using temperature-dependent reflectance data from literature sources and the comparison result was subsequently analyzed for reference. The second part of this study focused on the measurements of study [17], for which a feature-based approach was developed and applied to correct the reflectance drift and to account for the different effect of the redox-reactions with respect to the difference in the heating rates between the experiments in this study and the measurements in [17].

2 Experimental

2.1 Description of the setup

To validate the results of the reflectance measurements with the integrating sphere from [17], simulations were performed and validated with laser melting experiments conducted in a specifically developed welding chamber. To make the simulations and the experiments comparable, the

simulated processes had to be feasible for the experimental setup. For this reason, in the following, the setup and methods for the melting experiments are presented before the description of the model and methods for the melting simulations in section 3.

Figure 1 shows a schematic of the welding chamber. This setup mainly consisted of a vacuum chamber, in which the sample could be placed, preheated, and welded or melted without contact to atmospheric oxygen. Two automated linear stages (not depicted) inside the chamber allowed to move the sample two-dimensionally over the heating element. The two force vectors in the schematic represent the force that the fixture applied to the sample by the help of springs. This way, the copper sample was always pulled straight and slightly downwards to provide a reliable contact with the heating element and thus keep the sample in the focal distance of the laser, independent from the current lateral position and thermal expansion of the sample. The heating element, which was made from silicon nitride (Si_3N_4), featured a bore hole in the position of the laser spot to prevent the sample from being brazed to the heating element and to avoid damage of the heating element in case that the laser penetrates the melt pool of the sample. Two fine thermocouple wires of $80\ \mu\text{m}$ diameter contacted the upper surface of the sample to the left and the right of the bore hole. They did not contact each other directly and only formed the thermocouple through contact with the electrically conductive copper. This brought the material transition of the thermocouple

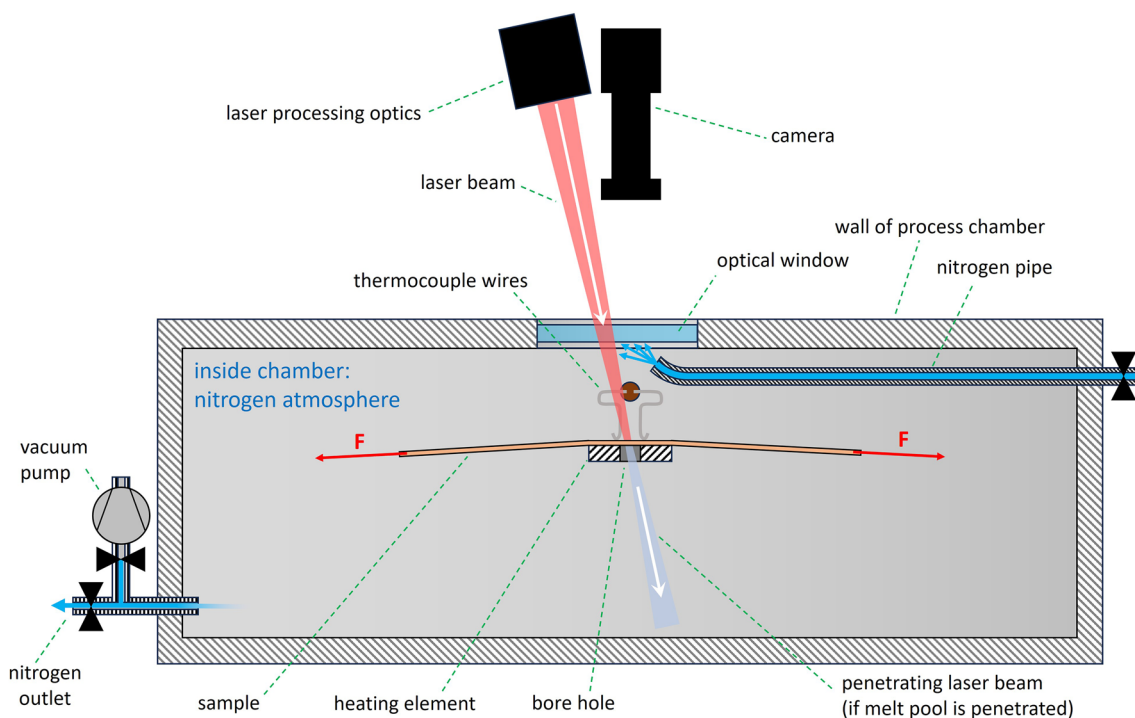


Fig. 1 Schematic of welding chamber

and thus the measurement position directly to the surface of the sample. It also prevented misleading measurements in situations with unstable surface contact, since the thermocouple only existed when both thermocouple wires were in electrical contact with the sample. The thermocouple wires stayed in a fixed position with respect to the laser spot and maintained electrical contact with the surface even when the sample was moved. The in-house developed temperature control system detected contact losses of the thermocouple wires, as they could occur when the sample moved, and kept the power supply for the sample constant at the average of the last seconds before the contact loss. Combined with the slow system response, this effectively avoided substantial temperature drifts in contact loss situations for durations up to 10 s. Contact losses for more than 10 s triggered an emergency shutdown procedure for the heating process to prevent possible overheating of the sample.

The laser source (not depicted) was an SLS 200 CL16 from Lasag. This flashlamp pumped Nd:YAG laser with 1064 nm wavelength was capable of temporal pulse shaping. The maximum pulse peak power of the laser at 4 ms pulse duration was approximately 3 kW. The laser constantly provided pulses at a set frequency into a power sink, while only the requested pulses were released into the fiber. According to the manufacturer, the combination of this constant pulsing and the real-time controlled power supply allows a pulse-to-pulse stability down to 0.5 %. The laser spot with top-hat intensity distribution on the sample surface originated from a 1:1 projection of the end of the 200 μm multimode delivery fiber (not depicted). The incident angle of the laser beam of 12° and the parallel orientation of the sample surface structure to the incident plane of the laser beam were in agreement with the arrangement during the reflectance measurements in the previous study of [17]. The camera provided the capability to take images of the laser spot position. However, the fixed working distance of 65 mm from the end of the camera lens to the sample surface limited the possible distance of the sample from the YAG-BBAR coated quartz glass window of 5 mm thickness, which allowed the camera to look into and the laser to penetrate into the chamber. To prevent degradations of the window due to weld splatter and other debris despite the short distance from the sample, a nitrogen pipe constantly blew nitrogen of the nominal purity class N5.0 onto the window throughout the laser melting procedure.

2.2 Laser melting experiments

Before the start of the experiments, a pure nitrogen atmosphere was established by three cycles of evacuation of the chamber down to 1.1e-1 mbar (abs) and of subsequent refilling to 1.05 bar (abs). Then, a constant nitrogen flow was established, the sample was heated to its designated initial

temperature, where required, and the automated laser melting process was started. This automated process repeated the melting process in a loop until all predefined laser-sample interactions of the experiment were executed. It first adjusted the laser pulse energy for the next processing position via the pulse peak power, then positioned the sample, took a pre-process image with the camera, triggered the release of a laser pulse, and finally took a post-process image of the processing result. The duration of 12 s per loop repetition allowed the laser to adapt to new pulse peak powers, allowed the temperature control to adapt to new positions of the sample, and allowed the sample to dissipate the locally absorbed energy from previous laser pulses to avoid heat accumulation. After the laser melting experiments, a microscope was used outside of the chamber to take another post-process image of each processing position on the sample. While the direct comparison of the grayscale post- and pre-process images from within the chamber allowed to distinguish sample modifications from pre-existing surface defects, the higher resolution color images from the microscope increased the accuracy at which modifications of the surface topography due to melting could be distinguished from other modifications such as color changes.

Out of all the sample types of the study in [17], the laser melting experiments in this study were only conducted with the untreated and the reduced sample types, both having a thickness of 0.1 mm, since the maximum pulse energies of the laser were insufficient to melt the polished and resolidified samples of a thickness of 1 mm. The samples in this study had lateral dimensions of 100 mm times 50 mm. They were cut from cold rolled sheets of electro tough-pitch copper (Cu-ETP or CW004A), which has a minimum copper content of 99.9 % and is commonly used in electrical applications. While the untreated samples were used as received, the reduced samples were heated in nitrogen atmosphere to approximately 1070 K to reduce the surface oxides. Table 1

Table 1 Overview of laser melting experiments

Temperature (in kelvins)	Pulse shape	Number of processing positions in each experimental instance	
		For reduced sample	For untreated sample
303	Ramp-up	651	651, 651, 630
	Flat-top	651, 651, 630	672, 672, 651
	Ramp-down	630	651, 651, 651, 651
503	Ramp-up	168	168
	Flat-top	168	168, 126
	Ramp-down	168	168
703	Ramp-up	168	168
	Flat-top	168	168
	Ramp-down	168	168

summarizes the laser melting experiments and their parameters. To find the melting pulse threshold energy for each combination of sample type, temperature, and pulse shape, the pulse peak power was increased in equal steps per processing position. The minimum and maximum power for each experimental instance was determined in pre-experiments of each 21 positions, in which the minimum value for the succeeding experiment was determined two power increments below the first melting event and the maximum value two power increments above the last melting event without piercing the metal. The exact number of processing positions for each experimental instance is listed in Table 1. Initially, 3 experimental instances were planned for each combination of sample type, temperature, and pulse shape. However, subsequent damages of several setup components and off-times due to electromagnetic interferences with a neighboring setup required to reduce the number of experimental instances and later even made it necessary to reduce the number of processing positions per instance in order to allow the conduction of at least 1 instance per experiment despite the resulting time shortage. To avoid selection bias and to keep the results as robust as possible, the results of all conducted experimental instances were kept in the study, including the accidentally conducted fourth instance with ramp-down pulse for the untreated sample at 303 K.

To prepare the simulations, the average laser power was measured over a duration of 20 s per power increment for set laser peak powers from 200 W to 6000 W in increments of 50 W. During each power measurement, the averaged temporal pulse profile was recorded over several consecutive pulses with a storage oscilloscope in combination with the built-in photodiode of the processing laser. The average laser power together with the set pulse repetition rate of the laser allowed to relate the pulse peak power for specific results to the pulse energy. Together with the recorded temporal pulse profile, it was also possible to calculate the temporal power profiles of the laser pulses, which were required as

input data for the simulations. This preparatory procedure was conducted for all three pulse shapes.

2.3 Data processing

The evaluation was divided into several steps and a tailored routine was used for each of them. The first routine calculated the temporal power profiles of the laser pulses from the pulse characterization measurements described above. To do so, this fully automated routine calculated the average pulse energy E_{pulse} for each combination of set pulse peak power and pulse shape:

$$E_{pulse} = \frac{P_{laser,mean}}{f_{pulse,set}} \tag{2}$$

Input data were the recorded average laser power $P_{laser,mean}$ from the power meter and the set pulse frequency f_{pulse} . Then, the routine calculated the time-dependent laser power $P(t)$ of the laser pulse by

$$P(t) = P(i * t_{inc}) = U(i * t_{inc}) * \frac{P_{laser,mean}}{f_{pulse,set} * \sum_{i=1}^{i_{end}} (U_i - U_{base}) * t_{inc}} \tag{3}$$

where U was the recorded voltage of the oscilloscope, U_i was the voltage of the recording increment i , U_{base} was the baseline voltage of the measurement, and t_{inc} was the uniform time increment between the measured voltages. i_{end} was the number of the last increment of each pulse shape dataset and equaled a value of 600 in all records. The result was the temporal power profile of the laser pulses, which was relevant for the simulations in this study. Before saving to the files, the routine smoothed the noise in the temporal power profiles by a moving average of 21 data points to improve the performance of the simulations. Figure 2 shows an example of the resulting temporal power profiles for each of the three

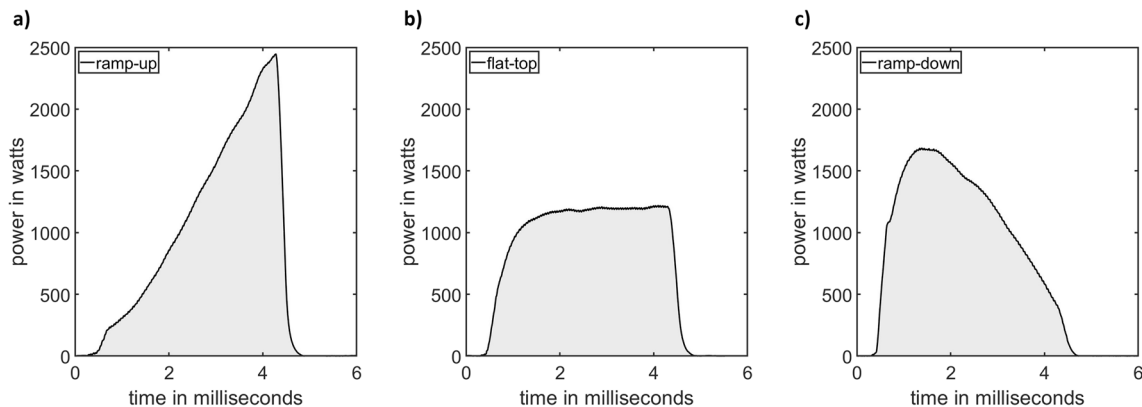


Fig. 2 Smoothened temporal power profiles of equal pulse energy (5.13 J) with different shapes of a ramp-up, b flat-top, and c ramp-down

pulse shapes, as they were used as input data for the simulations of this study. Although the three depicted pulses have the same pulse energy of 5.13 J and also have the same pulse duration of 4 ms, their pulse peak power differs significantly due to the different energy distribution over time.

The second routine evaluated the actual laser melting experiments. This semi-automatic routine required the operator to determine for each of the processed positions whether the applied pulse energy was sufficient to melt the sample or not. For this purpose, the routine presented the pre- and process image from the process camera in quick alternation to facilitate the identification of modifications by the laser pulse. It also presented the microscopic image of the same position on the sample that was taken by the hardness tester. The operator's response, whether the surface shows indications of melting, was saved in a list, together with the applied pulse energy from the process. This loop was repeated for all processing positions of a sample. The grayscale images from the process camera helped to decide whether a surface feature was the result of a surface modification due to the pulse, while the multispectral image of higher resolution from the hardness tester helped to better distinguish whether only the surface color or also the surface topology had changed. In case that the answer to the two image types did not agree, the operator could repeat the loop for the same processing position to take a final decision. Figure 3 shows an example of the microscopic image for pre-experiment 1, pre-experiment 2, and the first 189 out of 651 positions

for the main experiment of an untreated sample that was processed at 303 K with flat-top pulses. Positions with melt indications are marked with circles. The laser pulse energy was increased with the number of the processing position, which is indicated for the first and last position of each line.

The third routine determined the average melting threshold for each experiment by building a moving average over the melting status, where 1 equaled resolidified melt and 0 no melting event. This fully automated optimization routine increased the moving average length by one increment and restarted from the beginning until the moving average would not fall below 0.5 anymore after reaching it for the first time. The melting threshold was defined as the lowest pulse energy for which the optimized moving average was greater or equal 0.5. This way, the energy threshold for melting could be determined almost independently of the energy increment size between the processing positions. At the same time, the result was distinct despite the scattering of the results. Figure 4 shows an example of the result of the routine.

3 Simulations

3.1 Simulation model

The quality of the results from the temperature-dependent reflectance measurements was assessed with a simple finite element simulation model in Ansys Mechanical

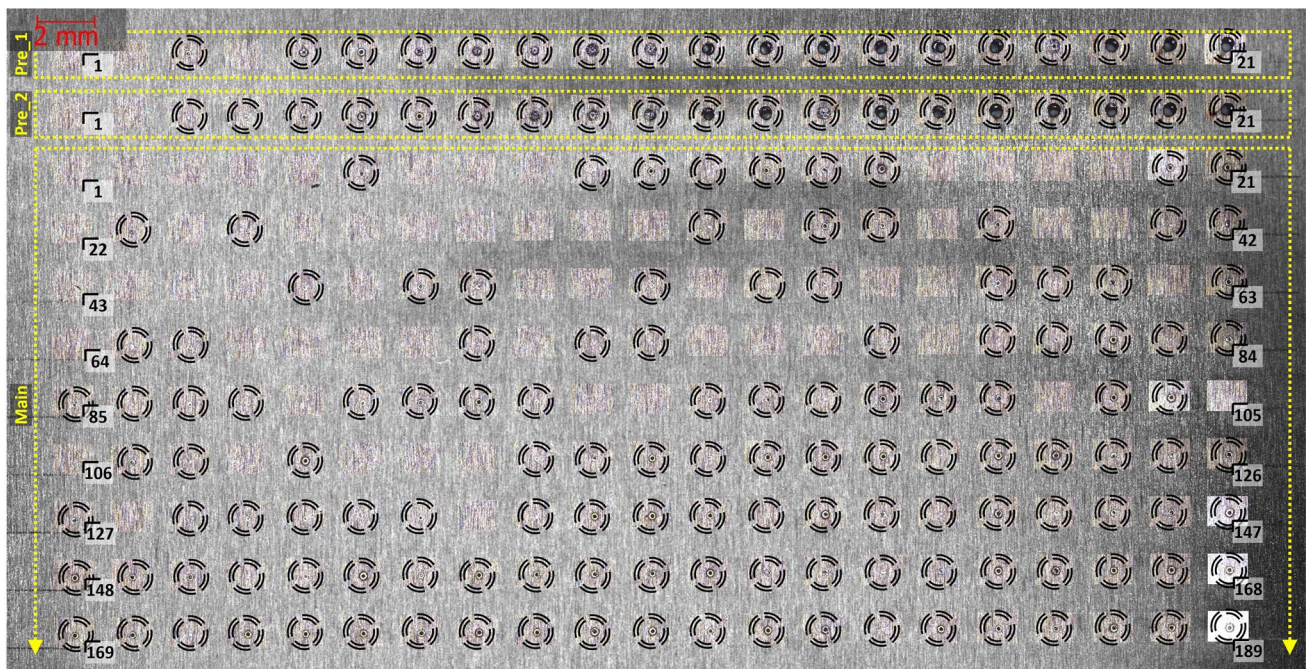


Fig. 3 Example of melt-positions marked with circles in the microscopic image for pre-experiment 1, pre-experiment 2, and the first 189 out of 651 positions of the main experiment, all processed with

flat-top pulse on the untreated sample type at 303 K (position numbers indicated for first and last position of each line)

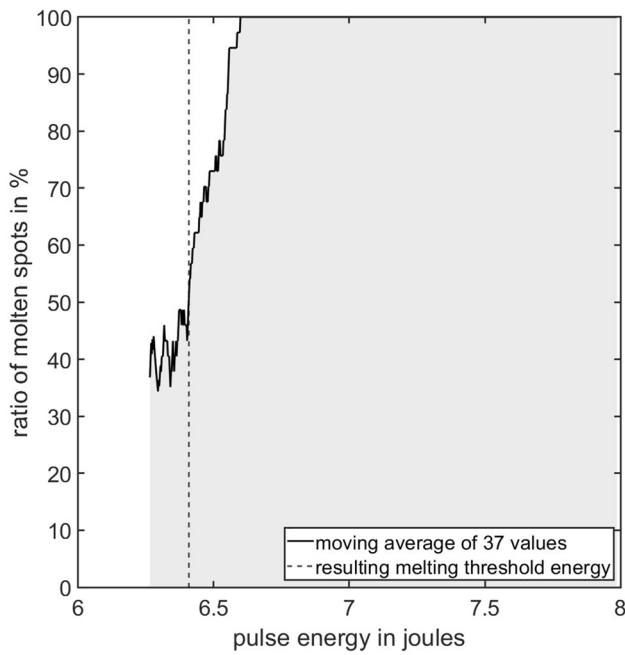


Fig. 4 Visualization of the melting threshold determination for the same sample as shown in Fig. 3, here for all 651 melt positions of the main experiment

APDL 19.1. Figure 5 shows the two-dimensional axisymmetric representation of the model, which basically was an advanced version of the simulation model in [18]. The model had a thickness of 100 μm. The whole model was meshed using Plane55 elements. From the symmetry axis

to a radius of 150 μm, the model strictly used the quadrilateral shape with a fixed edge length of 2 μm to obtain a good resolution in the area of interest. In the remaining area from 150 μm to the outer end of the model, which mainly served as a heat sink, the triangle shape with a variable edge length of up to 20 μm was used. The model had a fixed radius of 3 mm, which was determined through test simulations with varying radii before the beginning of the study, until it was just large enough to avoid temperature changes at the outer boundary throughout the laser pulse duration. This choice of radius allowed the model to effectively represent the behavior of significantly larger samples from the experiments until the end of the laser pulse, while excessive computation time during the simulation runs was avoided. The heat source of 100 μm radius in the topmost line of nodes (in red) represented a top hat laser spot with a diameter of 200 μm, as it was also used in the laser melting experiments. The heat source of the model implemented the temporal power profile of the pulses and the temperature-dependent absorptance by the equation:

$$\Phi_q(t, T) = \frac{(1 - R(T)) * P_{int}(t)}{\pi * \left(\frac{D_{Laser}}{2}\right)^2} \tag{4}$$

In this equation, $\Phi_q(t, T)$ was the heat flux which is generated by the heat source dependent on the time t and the local temperature T , $R(T)$ was the temperature-dependent reflectance of the sample, $P_{int}(t)$ was the time-dependent

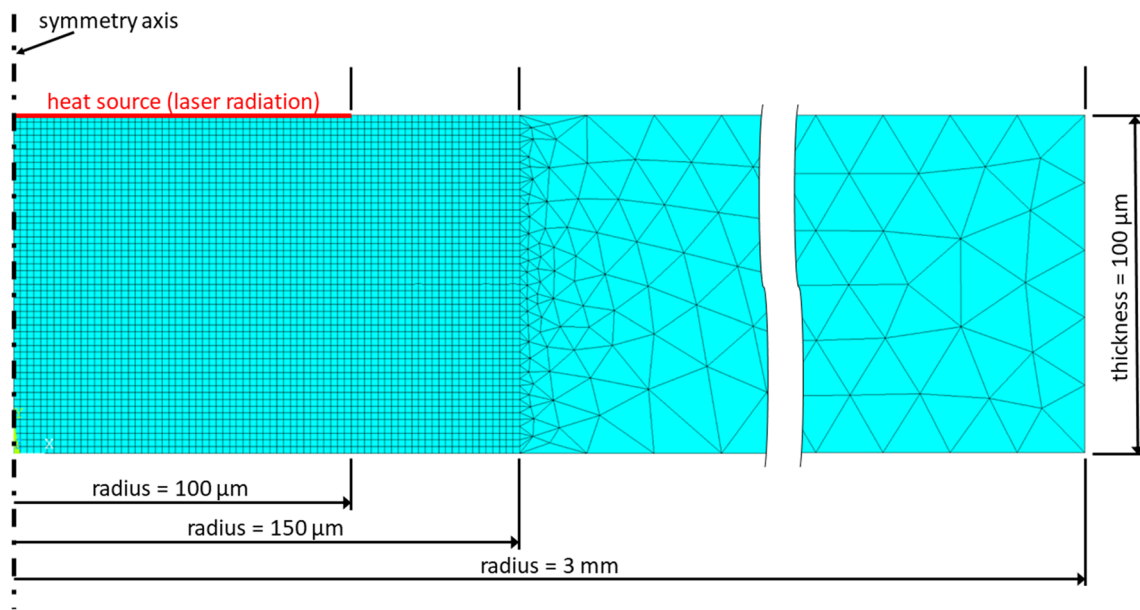


Fig. 5 Graphical representation of the FEM-model in Ansys mechanical

interpolated power of the laser pulse, and D_{Laser} was the diameter of the laser spot.

The melting temperature was set to 1357.77 K, in agreement with the definition of the international temperature scale of 1990 (ITS-90) [19]. In order to homogenize the temperature where melting effects occur, the melting temperatures for the enthalpy, thermal conductivity, and absorptance were adapted accordingly in all employed datasets. The volumetric enthalpy for the simulation input was calculated with

$$h_T^o - h_{298,15}^o \left(\frac{J}{m^3} \right) = \frac{\left[H_T^o - H_{298,15}^o \left(\frac{J}{mol} \right) \right]}{M_{Cu}} * \rho_{Cu} \quad (5)$$

where h is the volumetric enthalpy, H is the molar enthalpy from Arblaster [20], $\rho_{Cu} = 8.960 \text{ kg/m}^3$ is the relative density of copper from Speight [21] at 20 °C, and $M_{Cu} = 63.546043 * 10^{-3} \text{ (kg/mol)}$ is the molar mass. The molar mass was calculated with

$$M_{Cu} = N_A * m_u * A_r^o(Cu) \quad (6)$$

where $N_A = 6.02214076 * 10^{23} \text{ (mol}^{-1}\text{)}$ was the Avogadro-constant and $m_u = 1.6605402 * 10^{-27} \text{ (kg)}$ was the atomic mass unit, both after IUPAC [22]. $A_r^o(Cu) = 63,546$ was the standard atomic weight from Prohaska et al. [23]. The temperature-dependent thermal conductivity κ for the simulation was taken from Touloukian et al. [24]. To improve the stability of the simulations runs, the melting temperature was extended to a melting temperature range from

melting temperature to 20 K above melting temperature for the enthalpy and also the thermal conductivity. Figure 6 shows the results of these calculations as used in all simulations of this study.

Figure 7 a and b show the measured reflectance values for the untreated samples and the reduced samples from [17], respectively. The selected reflectance curve for the simulations in this study is highlighted in a darker red color. For the untreated samples, the reflectance curve with the highest data point density was selected, which also lies between the two others as the most representative one. For the reduced samples, which were reduced in nitrogen atmosphere before the reflectance measurements, the reflectance curve with the highest maximum temperature and the smallest reflectance dip around 1000 K was selected from the two agreeing curves. The black curve in each of the diagrams represents a temperature-corrected version of the selected curve, which was used in the corresponding simulations. The temperature correction was done by calibrating the temperature between the initial temperature and the theoretical melting temperature and applying a moving average to the temperature to reduce temperature noise. The averaging length was 10 values over time for the untreated sample and 50 values over time for the reduced sample, which was measured at a lower heating rate. The simulation loaded the temperature-dependent reflectance R from the temperature-corrected reflectance measurements in Fig. 7 and internally converted it to absorptance A by Eq. 1.

The simulation was carried out in a loop which automatically optimized the laser pulse energy, depending on whether

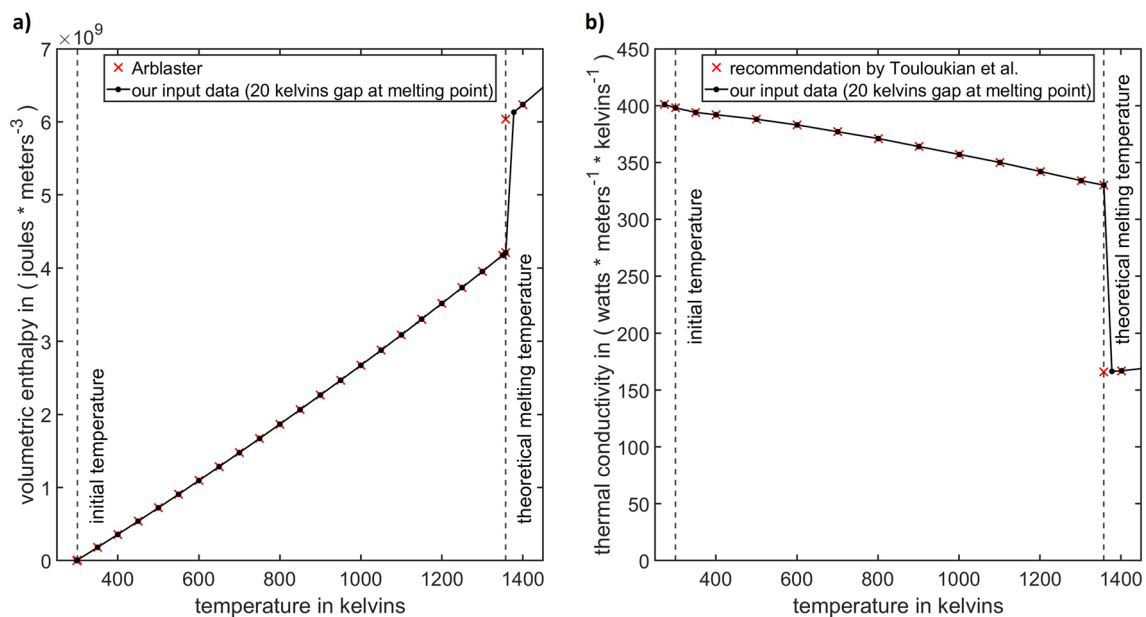


Fig. 6 Input data for the simulation model of this study with **a** volumetric enthalpy with respect to room temperature, based on Arblaster [20], and **b** thermal conductivity according to Touloukian [24]

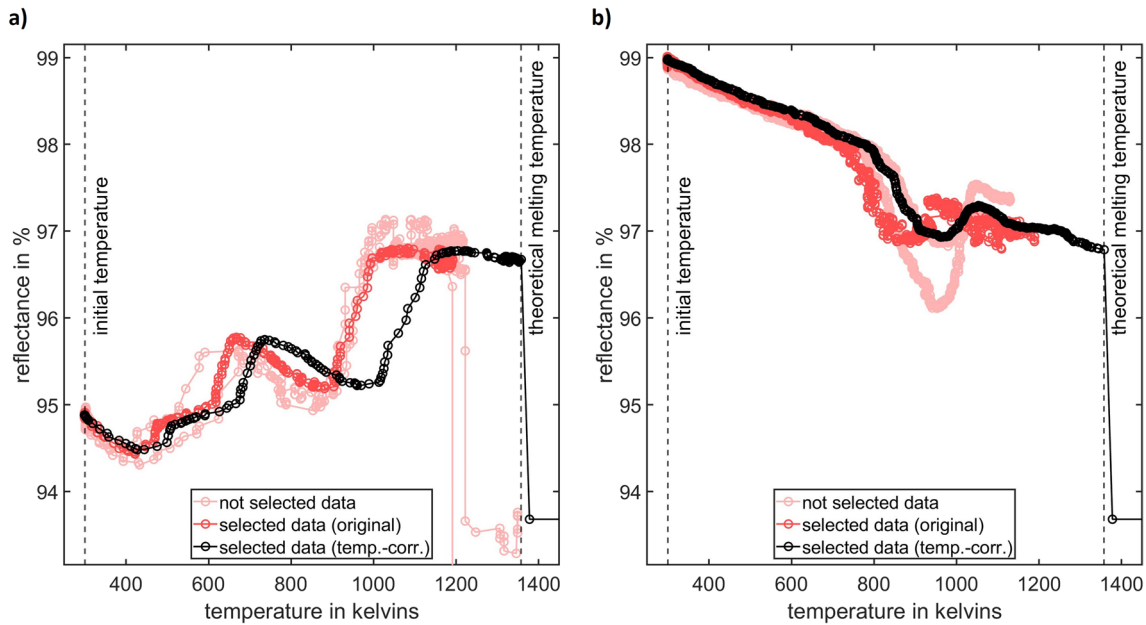


Fig. 7 Selected reflectance data from the measurements in [17] and their temperature-corrected version as used in the simulations of this study for **a** the untreated sample and **b** the reduced sample

the target temperature window was exceeded or not reached, by adding or subtracting an energy increment which was bisected with each repetition. The loop repeated until the highest temperature over all time steps in the center of the laser spot was between the melting temperature of 1357.77 K and the upper limit of a 10 K tolerance window at 1367.77 K. However, the database with the temporal power profiles for the different pulse shapes, which originated from the laser pulse measurements in the welding chamber, only provided data for certain discrete pulse energies. Therefore, at each iteration of the loop, the simulation loaded the temporal power profiles for the next existing lower and higher pulse energy and linearly interpolated the power values of the curves for each time position of the measurements. The resulting temporal power profiles represented the expected experimental pulse shape for the optimized laser pulse energy from the simulation.

The input data sources and starting conditions in the simulation script were manually adjusted for each simulated experiment. Then, the simulation was started and the pulse energy was automatically increased or decreased after each loop iteration until the maximum temperature of the current repetition met the tolerance criteria for the melting temperature. The pulse energy of this final loop was the pulse energy for the comparison with the required pulse energy in the experiments.

3.2 Comparison of simulations and experiments

The objective of this study was not to investigate the laser melting process itself, but to estimate the accuracy of the

various reflectance datasets through laser melting processes. The required laser power for melting is one of the most appropriate variables for this estimation, because it can be determined with high accuracy and because the absorbance and the absorbed power are directly proportional. This relationship means that the required laser power changes inversely proportional to the absorbance according to

$$P_{laser}(A) = \frac{P_{abs}}{A} \tag{7}$$

where P_{laser} is the laser power, P_{abs} is the absorbed laser power, and A is the absorbance as a fraction. However, a direct comparison of laser powers was not feasible, since the laser power was a time-dependent function in all recorded laser pulses and the exact temporal profile further depended on the pulse energy. Therefore, the required laser pulse energies as the integral of laser power over pulse duration were used for comparisons. A well-known approach to assess the prediction accuracy of a simulation is to calculate the agreement of the results in simulation and the experiment. Another approach is to calculate the required correction factor to bring the simulation result in alignment with the experimental result. Indeed, the correction factor is only the reciprocal value of the prediction accuracy, which is calculated by the ratio of simulation result over experimental result. But while the ranking order by absolute deviation from the ideal value of 1 is identical in both approaches when the simulations show only higher values or only lower values than the experiment, it can depend

on the chosen approach when simulations showing higher values and lower values than the experiment are compared with each other. However, the combined ranking of simulations showing higher values and lower values than the experiment is identical in both approaches if the logarithms of either agreement or correction factor are compared by their absolute values, where 0 is the ideal value. This way, ranking bias by the choice of the approach can be excluded. Since the logarithms of the agreement or the correction factor are difficult to interpret, the ranking plots in this study show the linear values of the results, but ranked by the absolute values of their logarithms. The simulations with different reflectance sets were not compared by the individual agreements for each of the 9 test cases, but by the averaged energy agreement of the melting threshold energy between simulations and experiments across the different test cases. It was calculated by

$$agr_{mean} = \frac{\sum_{i=1}^{i_{max}} \frac{E_{sim,i}}{E_{exp,i}}}{i_{max}} \quad (8)$$

where i was the index of the test case, $E_{sim,i}$ was the simulated energy of test case i , and $E_{exp,i}$ was the corresponding experimental energy of test case i . While the averaged energy agreement helps to determine to what extent the simulations over- or underestimated the experimental results on average, the relative standard deviation of the agreements for the different test cases gives information on how accurate the simulation represented the response of the experiment to changes in the process parameters.

4 Results

4.1 Validation of the measurements

Figure 8a shows the experimental results for the melting threshold energy of all experiments at the reduced samples, as specified in Table 1. The results of three experiments are visible for the flat-top pulse shape at 303 K. The experimental result for the flat-top pulse at 503 K equals the lower energy limit of the main experiment, since all processing positions in the main experiment were molten. Therefore, it does not result from a transition from predominantly non-molten positions to predominantly molten positions. However, the melting threshold in the two pre-experiments consistently fell within the energy limits of the main experiment. This led to the conclusion that the expected error is not substantial, taking into account the inherent limits of reproducibility in laser welding experiments on copper. Moreover, due to the time constraints mentioned in Section 2.2, repeating the experiments was not feasible without discarding other experiments of this study. Therefore, the

result was included in this study, but flagged accordingly to raise awareness. Additionally to the experimental results, Figure 8a shows the results for the simulations with each of the two temperature-corrected reflectance curves from Fig. 7 as input data and for simulations which use the reflectance curves from the literature. However, it was not possible to determine the melting energies at 303 K based on Quimby et al. [13], because even the measured temporal power profiles with the highest available pulse energy of the laser did not result in reaching melting temperature. On the other hand, the results set for Ujihara [10] is incomplete because the measured temporal power profile for the lowest available pulse energy of the laser still resulted in exceeding the melting temperature for the flat-top pulse at 703 K. All simulation results in the plot show the same general trends for the melt energies as the experimental results. But while the energies from simulations using the temperature-corrected reflectance values from Fig. 7 come in relatively close proximity with the experimental results, the energy from the simulations using the reflectance values from literature result in substantial deviations for the energies.

Figure 8b shows the averaged energy agreement of the simulations for each reflectance dataset with the experimental values for the reduced sample, as well as the reciprocal value of the agreement, which equals the correction factor. They are ranked by the absolute value of their logarithm. Figure 8c shows the relative standard deviation over the single agreements with the results on the reduced sample for each input dataset, ranked from the lowest to the highest relative standard deviation. Since the results sets for Quimby et al. [13] and for Ujihara [10] are incomplete, their calculated averaged energy agreement and relative standard deviation of the agreement are not fully representative. The simulation results with both of the reflectance data from Fig. 7 show the best averaged energy agreement among all data sources, but surprisingly, the averaged energy agreement of the results based on the reflectance of the untreated sample is better than the one of the results based on the reflectance of the reduced sample. The simulations using the reflectance values from Fig. 7 for the untreated sample underestimated the experimental energies on average by about 5 %, while the simulations using the reflectance values for the reduced sample overestimated the experimental energies on average by about 9 %. With regard to the relative standard deviation, the results for Quimby et al. [13] lead to the lowest value, indicating the best representation of the process response to the test cases. But, unfortunately, this standard deviation is not fully comparable, since the relative standard deviation could only be evaluated across 6 of 9 total test cases due to the power limits of the laser. The reflectance values for the reduced sample from Fig. 7 resulted in the second best representation of the process in terms of the standard

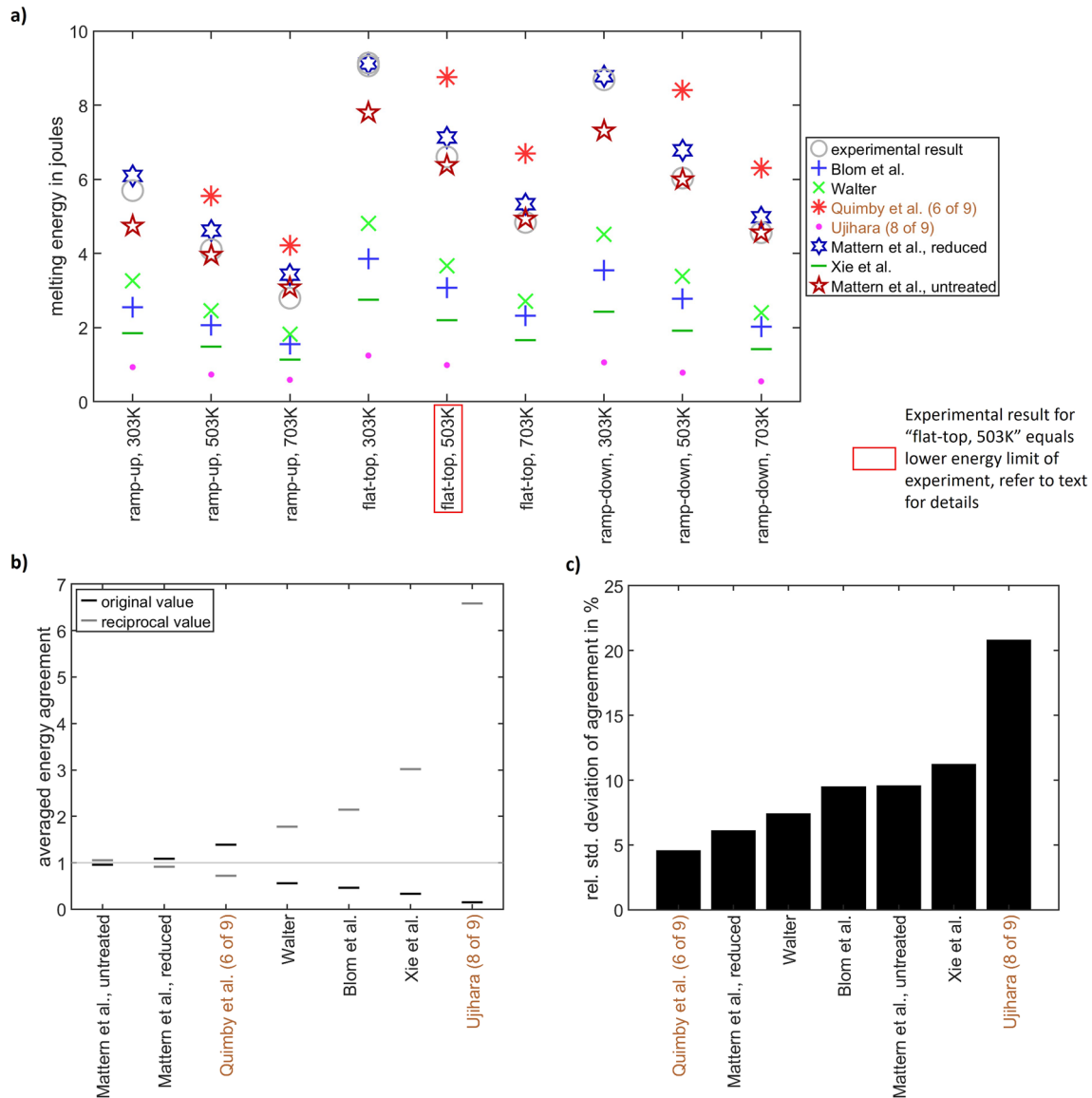


Fig. 8 a Melt energies from experimental results on reduced samples and from simulation results based on different input data for the reflectance, **b** averaged energy agreement of melting threshold energy

in simulations and experiments across the different test cases, **c** relative standard deviation of the agreements across the different test cases

deviation over the 9 test cases. The reflectance values for the untreated sample from Fig. 7 led to a significantly worse relative standard deviation which even exceeds the relative standard deviations resulting from the datasets of Walter and of Blom et al. from the literature.

Figure 9a shows the same results as Fig. 8a, but the experimental results for the reduced sample are replaced by the results of the untreated sample. The figure contains 3 results for each experiment at 303 K and 2 results for the experiment with the flat-top pulse at 503 K. The general response of the experimental results to the 9 test conditions is similar to that in the case of the reduced sample, but the melting energies are in general lower and the decrease of the melting

energies with increasing temperature is also lower. The averaged energy agreement between simulated and experimental melting threshold energies in Fig. 9b is the best for the simulations using the reflectance data for the untreated sample from Fig. 7, followed by the simulations using reflectance data for the reduced sample from Fig. 7 in position 3 of the ranking. Regarding the relative standard deviation of the individual agreements for the test cases, simulations using the reflectance values from Quimby et al. [13] again show the best agreement with the experimental process behavior. They are followed by simulations using the reflectance data from Fig. 7 for untreated copper and then for reduced copper.

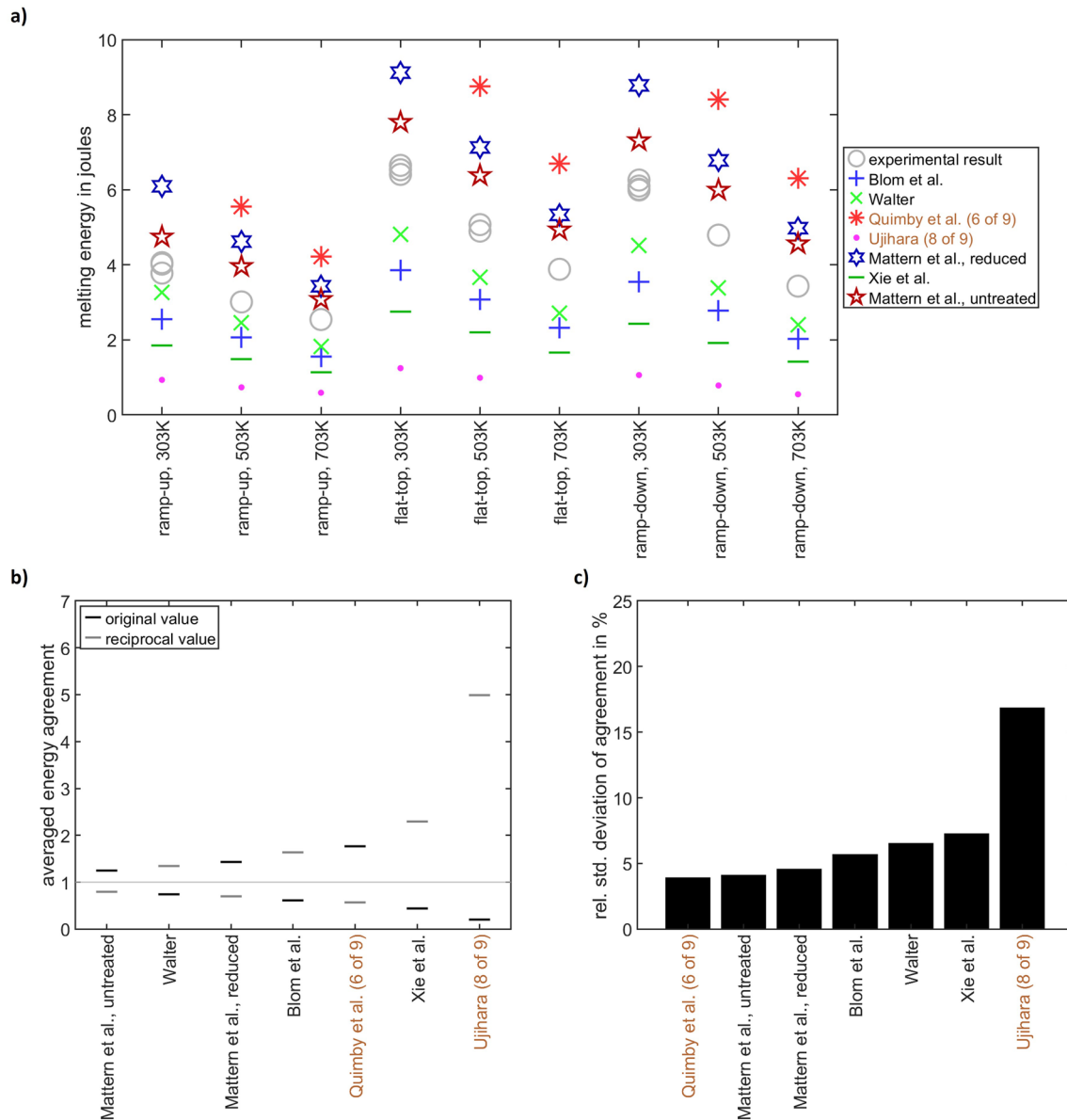


Fig. 9 **a** Melt energies from experimental results on untreated samples and from simulation results based on different input data for the reflectance, **b** averaged energy agreement of melting threshold energy

in simulations and experiments across the different test cases, **c** relative standard deviation of the agreements across the different test cases

Figure 8b and Fig. 9b show that the reflectance data for the untreated sample type from Fig. 7 led to the best averaged energy agreement between the simulated and the experimental melting threshold energies for the laser melting experiments with both sample types. Interestingly, the averaged energy agreement for simulations using the reflectance data for the reduced sample from Fig. 7 is worse, even for the experiment with the sample type on which the data were measured. Regarding the relative standard deviation and thus the representation of the process response to the different test cases, the simulations using the reflectance data for the respective sample type from Fig. 7 are only outperformed by those with

reflectance data from Quimby et al. [13], interestingly for the experiments with both sample types. However, the temperature-induced reflectance drift of the measurement setup and the challenge of the time-dependence of redox reactions has already been addressed in [17]. The following section deals with a solution for these two issues.

4.2 Process-oriented data corrections

This section presents a compensation strategy for the temperature-induced reflectance drift of the measurement setup and the time-dependence of the redox-reactions. The goal

of this strategy was to represent the reflectance curves over temperature during the laser melting experiments.

The reflectance drift in the measurements due to the temperature increase of the measurement setup can be assumed comparable for both sample types. On the other side, effects of the heating rate on results of the redox-reactions are more predictable for the reduced sample, since a perfectly reduced sample cannot undergo a further reduction of oxides, while the untreated sample still can. Also, no substantial oxidation has to be expected at sufficiently high heating rates or short processing times in nitrogen atmosphere. Therefore, the compensation strategy started with the reduced sample.

In the first step for the reduced sample, the reflectance dip at around 900 K was removed to account for the time-dependence of the redox-reaction. This was done because supplementary experiments in [17] show that oxidation takes time, which allows the conclusion that no substantial oxidation of the reduced sample will take place during the short processing time of the laser pulse. In the second step, the temperature-induced reflectance drift was compensated by shifting the reflectance of the remaining data points by 0 % at room temperature and by a defined percentage at the melting temperature. The reflectance shift for the data points in between was linearly interpolated over temperature. The reflectance shift at the melting temperature was adjusted until the agreement between the simulated and the experimental melting threshold energy was better than 1 %.

In the first step for the untreated sample, the same reflectance drift compensation was applied as for the reduced sample. This was done because the temperature-induced

reflectance drift of the setup is independent from the sample type. In the second step, the end point of the reduction-related reflectance increase was shifted to higher temperatures. Additionally, the reflectance of the new end point was reduced by the product of the magnitude of this shift and the general negative gradient of reflectance over temperature for copper in the measurements of [17]. The shift was adjusted until the agreement between the simulated melting threshold energy and the experimental melting threshold energy was better than 1 % for the untreated sample, too.

Figure 10a shows the solely temperature-corrected together with the fully corrected reflectance curve for the reduced sample, both including the values for the melted copper. The simulated melting threshold energy showed the best agreement for a reflectance shift at melting temperature of -0.4 %, which is consistent with the analysis of the cooling curves in [17]. The averaged energy agreement of the simulated and the experimental melting threshold energy over all 9 test cases worsened from 1.0922 with the solely temperature-corrected reflectance data to 1.1127 with additionally neglected redox-effects and then improved to 1.0034 after the compensation of the temperature-induced reflectance drift. The relative standard deviation worsened from 6.13 % for the solely temperature-corrected reflectance curve to 6.18 % with additionally neglected redox-effects and then improved to 6.12 % for the fully corrected reflectance, which is comparable to the value for the solely temperature-corrected reflectance curve.

Figure 10b shows the solely temperature-corrected together with the corrected reflectance curve for the

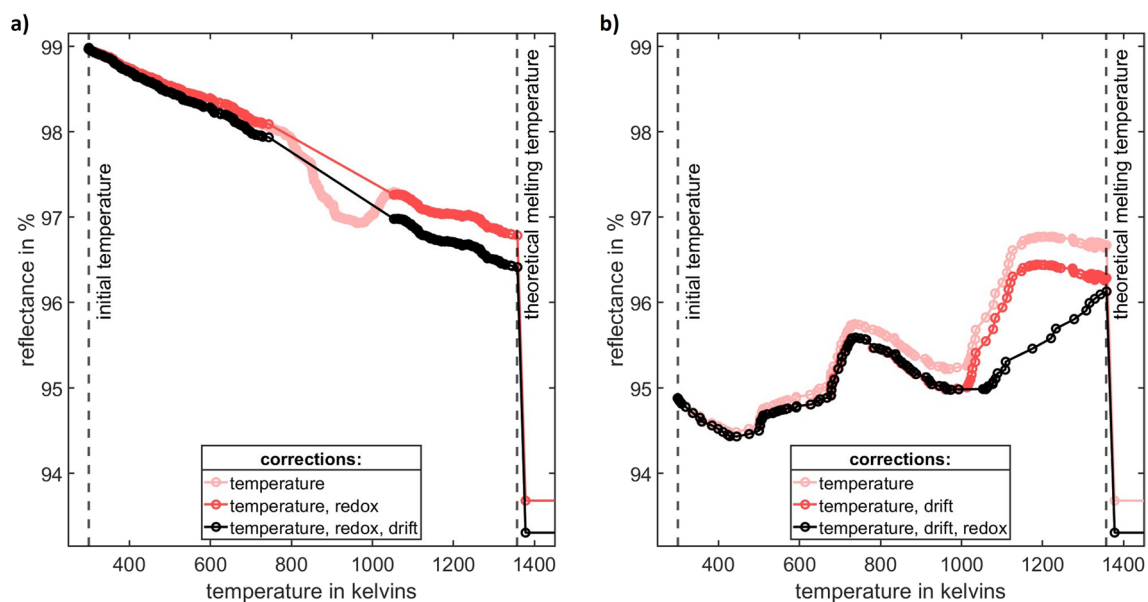


Fig. 10 Reflectance with different levels of correction for temperature errors, temperature-induced reflectance drift and differences in redox-reactions of **a** reduced sample and **b** untreated sample

untreated sample, both including the values for the melted copper. After the compensation of the temperature-induced reflectance drift by -0.4% , the simulated melting threshold energy showed the best agreement for a shift of the end point of the reduction-related reflectance by $+250\text{ K}$. The averaged energy agreement of the simulated with the experimental melting threshold energy over all 9 test cases improved from 1.2497 with the solely temperature-corrected reflectance data to 1.1296 after the additional compensation of the reflectance drift and then further improved to 1.0031 after the adaptation of the slope for the oxide reduction. The relative standard deviation improved from 4.12% with the solely temperature-corrected reflectance data to 3.88% after the compensation of the reflectance drift and then improved even more to 3.78% after the adaptation of the slope for the oxide reduction.

For both samples, the compensation strategy helped to bring the averaged energy agreement of the simulated melting energies and the experimental melting energies into nearly perfect agreement. The exclusive removal of the reflectance drop for the reduced sample led to a worsened averaged energy agreement. This is most likely a consequence of the resulting reduction of the absorbed power, which was already too low with the solely temperature-corrected reflectance data. However, the following compensation of the temperature-induced reflectance drift increased the absorbed power and consequently led to the nearly perfect averaged energy agreement of the simulated and the experimental melting energies. The relative standard deviation, which after the application of the full compensation strategy is nearly identical to before, indicates that the compensation did not affect the representation of the process behavior in a negative way. Together with the improved averaged energy agreement, the compensation strategy can therefore be regarded as successful for the reduced sample. The relative standard deviation is still better for simulations using reflectance data from Quimby et al. [13], but it is important to note that the standard deviation based on this reflectance is not fully comparable to the other standard deviations since it does not comprise results at room temperature. In the case of the untreated sample, both elements of the compensation strategy had positive effects on the agreement between the simulated melting energies and their experimental counterparts. Also, the relative standard deviation improved after each of the two steps, which means that both steps improved the representation of the experimental process by the simulation. The compensation strategy can therefore also be regarded as successful for the untreated sample. The relative standard deviation for the untreated sample after the application of the compensation strategy is even better than the one of Quimby et al. [13], which was not the case with the uncompensated data.

The temperature-induced reflectance-drift is a purely setup-related measurement error, and its compensation is therefore purely setup-related as well, independent from the intended usage of the data. However, the error due to differences in the redox-reactions between the reflectance measurements and the laser melting experiments is in fact no measurement error, but results from existing modifications of the sample. Since these modifications are sample-related and depend on the oxygen partial pressure and the heating rate, the adaptation of the reflectance data has to be conducted specifically for the conditions of the simulated experiment. Therefore, the adjustment of effects from redox-reactions in the reflectance data might need to be recalculated, and in some cases, even the compensation strategy might need to be adapted in order to represent the reflectance curves during experiments with significantly different process parameters. While general correction factors, as they are often used in simulations, simply multiply all values of a specified variable by the same factor, the compensation strategy in this study improves the input data quality. This does not only improve the averaged energy agreement of simulation results with the experimental results, but it also results in an improved representation of the process response to changes in process parameters, which is demonstrated through the reduced relative standard deviation.

5 Conclusions

The study successfully used a combined approach of simulations and experiments to assess and then improve the data quality of temperature-dependent reflectance measurements from [17] for untreated or reduced sheets of electro tough pitch copper. The simulations and experiments for each dataset or sample type covered the same 9 test cases, which were combinations of 3 different sample temperatures and 3 different laser pulse shapes. Comparisons of the melting threshold energy before the improvement already revealed a superior agreement of the simulations with the experimental results when the simulations were conducted using the measured temperature-dependent reflectance from [17] instead of values from literature sources. Only simulations with the data from Quimby et al. [13] resulted in an even smaller standard deviation, but the simulations with these data only covered 6 out of 9 test cases and were therefore not fully comparable. The compensation of the temperature-induced reflectance drift in the measurements and the adaptation of redox-effects in the reflectance to the heating rate during the laser melting experiments resulted in even better agreements for the simulation results with the experiments. Overall, the presented approach demonstrates the importance of sample-specific reflectance measurements for copper surfaces

in order to reach representative results for laser welding simulations. The conducted compensation strategy further increased the precision of available reflectance data to an unprecedented level that will be useful for a deeper understanding of the challenges in laser welding of copper.

Acknowledgements Lalit Mohan Kukreja thanks Alexander von Humboldt Foundation of Germany for the follow-up program fellowship for his collaboration with our institute. We thank the institute for materials at the Ruhr-University Bochum for providing us the microscope, which was used for automated post-process imaging of the samples. We further thank our colleagues Jan Hoppius and Philipp Maack for their assistance with the development of the temperature controls for the integrating sphere setup and the welding setup. We thank Christian Hiltner from the chair of thermodynamics and Michael Niesen from the institute of thermo and fluid dynamics for their support regarding the electrical safety of our setups.

Funding Open Access funding enabled and organized by Projekt DEAL. This study is funded by the Deutsche Forschungsgemeinschaft (DFG, German Research Foundation) – 261897876.

Declarations

Conflict of interests The authors declare no competing interests.

Open Access This article is licensed under a Creative Commons Attribution 4.0 International License, which permits use, sharing, adaptation, distribution and reproduction in any medium or format, as long as you give appropriate credit to the original author(s) and the source, provide a link to the Creative Commons licence, and indicate if changes were made. The images or other third party material in this article are included in the article's Creative Commons licence, unless indicated otherwise in a credit line to the material. If material is not included in the article's Creative Commons licence and your intended use is not permitted by statutory regulation or exceeds the permitted use, you will need to obtain permission directly from the copyright holder. To view a copy of this licence, visit <http://creativecommons.org/licenses/by/4.0/>.

References

- Ralls KM, Courtney TH, Wulff J (1976) Introduction to materials science and engineering. John Wiley & Sons, Inc
- Biro E, Weckman DC, Zhou Y (2002) Pulsed Nd YAG laser welding of copper using oxygenated assist gases. *Metall Mater Trans A* 33:2019–2030. <https://doi.org/10.1007/s11661-002-0034-4>
- Hummel M, Schöler C, Häusler A et al (2020) New approaches on laser micro welding of copper by using a laser beam source with a wavelength of 450 nm. *J Adv Join Process* 1:100012. <https://doi.org/10.1016/j.jajp.2020.100012>
- Helm J, Schulz A, Olowinsky A et al (2020) Laser welding of laser-structured copper connectors for battery applications and power electronics. *Weld World* 63:109. <https://doi.org/10.1007/s40194-020-00849-8>
- Zięba A, Maj P, Siwek M et al (2023) Analysis of thermally grown oxides on microperforated copper sheets. *J Mater Eng Perform.* <https://doi.org/10.1007/s11665-023-08328-z>
- Schöler C, Nießen M, Hummel M et al (2019) Modeling and simulation of laser micro welding. In: *Proceedings of Lasers in Manufacturing Conference 2019*
- Heider A, Stritt P, Hess A et al (2011) Process stabilization at welding copper by laser power modulation. *Phys Procedia* 12:81–87. <https://doi.org/10.1016/j.phpro.2011.03.011>
- Kawahito Y, Katayama S (2004) In-process monitoring and feedback control during laser microspot lap welding of copper sheets. *J Laser Appl* 16:121–127. <https://doi.org/10.2351/1.1710885>
- Otto A, Vázquez RG, Hartel U et al (2018) Numerical analysis of process dynamics in laser welding of Al and Cu. *Procedia CIRP* 74:691–695. <https://doi.org/10.1016/j.procir.2018.08.040>
- Ujihara K (1972) Reflectivity of metals at high temperatures. *J Appl Phys* 43:2376. <https://doi.org/10.1063/1.1661506>
- Walter WT (1980) Reflectance changes of metals during laser irradiation. In: Ready JF (ed) *Laser Applications in Materials Processing: Proc. SPIE*. SPIE, pp 109–119. <https://doi.org/10.1117/12.958027>
- Xie J, Kar A, Rothenflue JA et al (1997) Temperature-dependent absorptivity and cutting capability of CO₂, Nd:YAG and chemical oxygen-iodine lasers. *J Laser Appl* 9:77–85. <https://doi.org/10.2351/1.4745447>
- Quimby RS, Bass M, Liou L (1983) Calorimetric measurement of temperature dependent absorption in copper. In: Bennett HE, Guenther AH, Milam D et al (eds) *Laser induced damage in optical materials: 1981*. ASTM International, 100 Barr Harbor Drive, PO Box C700, West Conshohocken, PA 19428-2959, pp 142–151. <https://doi.org/10.1520/STP372365>
- Blom A, Dunias P, van Engen P et al (2003) Process spread reduction of laser microspot welding of thin copper parts using real-time control. In: Pique A, Sugioka K, Herman PR et al (eds) *Photon Processing in Microelectronics and Photonics II*. SPIE, pp 493–507. <https://doi.org/10.1117/12.478612>
- Siegel E (1976) Optical reflectivity of liquid metals at their melting temperatures. *Phys Chem Liq* 5:9–27. <https://doi.org/10.1080/00319107608084103>
- Kohl S, Kaufmann F, Schmidt M (2022) Why color matters—proposing a quantitative stability criterion for laser beam processing of metals based on their fundamental optical properties. *Metals* 12:1118. <https://doi.org/10.3390/met12071118>
- Mattern M, Kukreja LM, Ostendorf A (2023) Temperature-dependent reflectance of copper with different surface conditions measured at 1064 nm. *J Mater Eng Perform.* <https://doi.org/10.1007/s11665-023-08961-8>
- Mattern M, Weigel T, Ostendorf A (2018) Temporal temperature evolution in laser micro-spot welding of copper considering temperature-dependent material parameters. *Mater Res Express* 5:66545. <https://doi.org/10.1088/2053-1591/aacc3a>
- Preston-Thomas H (1990) The international temperature scale of 1990 (ITS-90). *Metrologia* 27:3–10. <https://doi.org/10.1088/0026-1394/27/1/002>
- Arblaster JW (2015) Thermodynamic properties of copper. *J Phase Equilibria Diffus* 36:422–444. <https://doi.org/10.1007/s11669-015-0399-x>
- Speight JG (2017) *Lange's handbook of chemistry*, 17th edn. McGraw-Hill Education, New York
- IUPAC (1997) *Compendium of chemical terminology: the "Gold Book"*, 2nd edn. Blackwell Scientific Publications, Oxford. <https://doi.org/10.1351/goldbook.A00497>
- Prohaska T, Irrgeher J, Benefield J et al (2022) Standard atomic weights of the elements 2021 (IUPAC Technical Report). *Pure Appl Chem* 94:573–600. <https://doi.org/10.1515/pac-2019-0603>
- Touloukian YS, Powell RW, Ho CY et al (1978) Thermal conductivity: metallic elements and alloys. In: *Thermophysical properties of matter - The TPRC data series, vol 1*, 3rd edn. IFI/Plenum, New York

Publisher's Note Springer Nature remains neutral with regard to jurisdictional claims in published maps and institutional affiliations.